Nuclear Inst. and Methods in Physics Research, A 1041 (2022) 167359

Contents lists available at ScienceDirect

Nuclear Inst. and Methods in Physics Research, A

journal homepage: www.elsevier.com/locate/nima

Assembly and performance of SiPM arrays for the prototype SCT proposed for CTA

G. Ambrosi [a,*], M. Ambrosio [b], C. Aramo [b], W. Benbow [c], B. Bertucci [a,d], E. Bissaldi [e,f], M. Bitossi [g], A. Boiano [b], C. Bonavolontà [b], R.A. Cameron [h], M. Capasso [i], L. Consiglio [b], D. Depaoli [j,k], F. Di Pierro [k], L. Di Venere [e,f], E. Fiandrini [a,d], A. Furniss [l], A. Gent [m], N. Giglietto [e,f], F. Giordano [e,f,*], W. Hanlon [c], O. Hervet [n], S. Incardona [o,p], M. Ionica [a], W. Jin [q], D. Kieda [r], F. Licciulli [f], S. Loporchio [f,*], G. Marsella [o,p], V. Masone [b], B.A.W. Mode [s], R. Mukherjee [i], F.R. Pantaleo [e,f], R. Paoletti [g,t], D. Ribeiro [u], A. Rugliancich [g], L. Saha [c], L. Stiaccini [t,g], L.P. Taylor [s], L. Tosti [a,d], G. Tripodo [o,p], V. Vagelli [a,v], M. Valentino [b,w], J. Vandenbroucke [s], V.V. Vassiliev [x], D.A. Williams [n]

[a] INFN Sezione di Perugia, 06123 Perugia, Italy
[b] INFN Sezione di Napoli, 80126 Napoli, Italy
[c] Center for Astrophysics — Harvard & Smithsonian, Cambridge, MA 02138, USA
[d] Dipartimento di Fisica e Geologia dell'Università degli Studi di Perugia, 06123 Perugia, Italy
[e] Dipartimento Interateneo di Fisica dell'Università e del Politecnico di Bari, 70125 Bari, Italy
[f] INFN Sezione di Bari, 70125 Bari, Italy
[g] INFN Sezione di Pisa, 56127 Pisa, Italy
[h] Kavli Institute for Particle Astrophysics and Cosmology, SLAC National Accelerator Laboratory, Stanford University, Stanford, CA 94025, USA
[i] Department of Physics and Astronomy, Barnard College, Columbia University, NY 10027, USA
[j] Dipartimento di Fisica dell'Università degli Studi di Torino, 10125 Torino, Italy
[k] INFN Sezione di Torino, 10125 Torino, Italy
[l] Department of Physics, California State University - East Bay, Hayward, CA 94542, USA
[m] School of Physics & Center for Relativistic Astrophysics, Georgia Institute of Technology, Atlanta, GA 30332-0430, USA
[n] Santa Cruz Institute for Particle Physics and Department of Physics, University of California, Santa Cruz, CA 95064, USA
[o] Dipartimento di Fisica e Chimica "E. Segrè", Università degli Studi di Palermo, 90128 Palermo, Italy
[p] INFN Sezione di Catania, 95123 Catania, Italy
[q] Department of Physics and Astronomy, University of Alabama, Tuscaloosa, AL 35487, USA
[r] Department of Physics and Astronomy, University of Utah, Salt Lake City, UT 84112, USA
[s] Department of Physics and Wisconsin IceCube Particle Astrophysics Center, University of Wisconsin, Madison, WI 53706, USA
[t] Dipartimento di Scienze Fisiche, della Terra e dell'Ambiente, Università degli Studi di Siena, 53100 Siena, Italy
[u] Physics Department, Columbia University, New York, NY 10027, USA
[v] Agenzia Spaziale Italiana, 00133 Roma, Italy
[w] CNR-ISASI, 80078 Pozzuoli, Italy
[x] Department of Physics and Astronomy, University of California, Los Angeles, CA 90095, USA

ARTICLE INFO

Keywords:
Silicon photomultipliers
Cherenkov telescopes array
Very-high-energy astrophysics

ABSTRACT

The Near Ultraviolet High Density (NUV-HD) SiPMs produced by Fondazione Bruno Kessler have been employed to develop 16-pixel optical units to equip the focal plane of the prototype Schwarzschild–Couder Telescope (pSCT) proposed as a possible design for the Medium-Sized Telescope of the Cherenkov Telescope Array Observatory. After the assembly procedure, the optical units were tested and characterized to study their performance and homogeneity in terms of gain and dark count rate. In this work, we report on the assembly procedure and on the laboratory tests performed on different production of NUV-HD and the selection we made for the best quality sensors to be used in the installation on the telescope camera. Currently 36 NUV-HD3 optical units have been successfully integrated on the pSCT camera, together with 64 HAMAMATSU MPPCs. An upgrade of the pSCT camera is foreseen over the next years when the full focal plane is expected to be equipped entirely with FBK NUV-HD3 SiPMs, for a total of 11328 pixels.

* Corresponding authors.
E-mail addresses: giovanni.ambrosi@pg.infn.it (G. Ambrosi), francesco.giordano@ba.infn.it (F. Giordano), serena.loporchio@ba.infn.it (S. Loporchio).

https://doi.org/10.1016/j.nima.2022.167359
Received 22 April 2022; Received in revised form 26 July 2022; Accepted 31 July 2022
Available online 12 August 2022

1. Introduction to the pSCT camera

The Cherenkov Telescope Array (CTA)[1] will represent the new generation of Imaging Atmospheric Cherenkov Telescopes (IACTs), aimed at the detection of very-high-energy (VHE) gamma rays by collecting the ultraviolet (UV) and visible Cherenkov light produced in gamma-ray induced electromagnetic showers in the atmosphere. These cosmic gamma rays represent a unique probe for a large number of physical phenomena, ranging from cosmic rays physics, astrophysics to fundamental physics [1]. The basic technique of IACT consists in focusing the Cherenkov radiation emitted by air showers into a fast photo-sensor camera for indirect measurements of gamma rays at the ground. A large number of photon detectors is necessary to reconstruct a shower image with high precision to perform the reconstruction of the events. This technique exploits the atmosphere as a calorimeter, where the air shower is generated and Cherenkov radiation is emitted. By studying the Cherenkov light on the ground, it is possible to reconstruct the energy and arrival direction of the incoming VHE gamma-ray.

CTA is planning to install about 100 telescopes with different configurations and acceptance in two observatories, one in the northern and one in the southern hemisphere, in order to achieve the full-sky coverage and increase the detection area and the detection rates [2]. The northern site will be built at the Observatorio del Roque de los Muchachos on the island of La Palma in the Canary Islands (Spain), while the southern one will be built in the vicinity of the existing Paranal Observatory in the Atacama Desert in Chile.

The energy range of CTA will extend over four energy decades, from tens of GeV up to hundreds of TeV, in order to overlap with the space-borne gamma-ray detector energy range and investigate the gamma-ray sky at the highest energies [3]. If compared to current IACT facilities, the CTA Observatory will extend the flux sensitivity by at least one order of magnitude in the core energy range. In order to provide broad energy coverage and improve the performance over the wide energy range foreseen for CTA, telescopes will be built in three classes with different sizes: Large-Sized Telescopes (LSTs) for the lower energies (up to a few hundred of GeV), Medium-Sized Telescopes (MSTs) for the core energy range and Small-Sized Telescopes (SSTs) to detect gamma rays above a few TeV.

A large number of MSTs will populate the inner part of each array, improving the angular and energy resolutions. Two different MST designs have been proposed: the traditional single mirror Davies–Cotton MST (DC-MST) [4] and the dual mirror Schwarzschild–Couder MST (SCT) [5]. With a two-mirror optical design, the SCT allows spherical and comatic aberrations to be corrected, opening the possibility to instrument the telescope with a compact and high-resolution camera [6].

A prototype of the Schwarzschild–Couder Telescope (pSCT) is being developed at the Fred Lawrence Whipple Laboratory in Arizona (USA). Its camera design is based on Silicon PhotoMultiplier (SiPM) sensors grouped in Photon Detection Units (PDU). Over the past 10 years, a joint venture between several Italian Universities, the Italian National Institute for Nuclear Physics (INFN), the Italian National Institute for Astrophysics (INAF), Fondazione Bruno Kessler (FBK) and various industrial partners have joined the efforts to design and develop SiPM arrays compatible with the already existing pSCT camera mechanical structure and readout electronics.

The pSCT camera has a width of 81 cm for a total field of view of 8° and will host 11 328 sensors, each one corresponding to a 0.064° pixel in the sky, matching the Point Spread Function (PSF) of the optical system [8]. The pSCT camera has a modular concept based on $54 \times 54\,\mathrm{mm}^2$ area PDUs, each one divided into 4 optical modules composed of sixteen $6 \times 6\,\mathrm{mm}^2$ SiPM sensors [7]. From now on, we will refer to the 16-SiPM optical modules as *SiPM arrays*. The whole camera is composed of 708 SiPM arrays, arranged into 177 PDUs. The schematic of the focal plane is shown in Fig. 1.

At the time of writing, the optical system of the pSCT is fully functional and the optical alignment system is currently undergoing commissioning [9]. At the moment, only the central sector of the pSCT camera has been installed: 16 PDUs of it have been equipped with Hamamatsu S12642-0404PA-50(X) MPPC modules, while the remaining 9 PDUs, corresponding to 36 SiPM arrays, are equipped with FBK SiPMs to verify their performance towards an upgrade of the pSCT camera based entirely on such devices. In the context of the assembly of PDUs for the pSCT, different FBK devices have been used as a benchmark for the development of the assembly and test procedures [10].

Near UltraViolet High-Density (NUV-HD) SiPMs manufactured by FBK are devices specifically designed and optimized for blue and near ultraviolet light detection. Over the years, the technology was improved with the aim of detecting the Cherenkov emission, leading to the final design used for the pSCT camera. More details regarding the optimization of the SiPM structure for blue light detection can be found in [11–13]. The first results regarding the characterization of FBK NUV-HD SiPMs with an area of $6 \times 6\,\mathrm{mm}^2$ and pitch of 30 μm are reported in [14]. The evolution of the technology over the years led to the production of SiPMs with the same area of $6 \times 6\,\mathrm{mm}^2$ and an increased pitch of 40 μm, which were renamed NUV-HD3 SiPMs. Three different consecutive productions of these devices were used to test and develop the PDUs for pSCT: HD3-2, HD3-3, and HD3-4. The productions mainly differ by the quality of the silicon substrates, which results in a different rate of dark counts. Details about the FBK SiPMs' electrical characterization and mechanical structure are reported in [14–16].

A thorough characterization measurement campaign was carried out to measure the SiPMs gain, Photon Detection Efficiency (PDE), cross-talk probability and dark count rate, including the temperature dependencies of all these quantities, and is presented in [17]. The measurements allowed to select the best device to be installed on the pSCT camera, namely HD3-4 (from now on, simply HD3). In particular, when biased 5 V above the breakdown, these devices proved to have a cross-talk probability of about 20%, a dark count rate of about 3 MHz over an active surface of 36 mm^2 and a PDE at 400 nm almost up to 55%. Nine PDUs equipped with HD3-4 have been instead fully integrated into the pSCT camera.

The paper is organized as follows. In Section 2 we introduce the design of the PDU tiles, along with their mechanical and electrical aspects. In Section 3 we describe the custom assembly procedure of a total of 150 SiPM arrays of different productions and the electrical tests performed at INFN Perugia in order to verify the quality of the sensors and the uniformity of the breakdown voltages. In Section 4 we describe the uniformity tests we performed at INFN Bari on each array, presenting the performance in terms of gain, Signal-to-Noise ratio (SNR), and Dark Count Rate (DCR). In total, 48 SiPM arrays were produced and tested, among which we selected the 36 arrays necessary to equip the 9 PDUs of the pSCT camera. Finally, in Section 5 we provide a summary of the measurements presented in the paper, along with the first scientific results of the pSCT camera, introducing the upgrade foreseen over the next years.

2. Design of PDU tiles

We designed custom $26.8 \times 26.8\,\mathrm{mm}^2$ area tiles to host the SiPMs in order to be compatible with the pSCT camera design [10]. The concept of the printed circuit board (PCB) tile was designed to maximize the homogeneity of the active area over the mechanical camera area, implementing safety dead areas for the assembly. Modules populate the pSCT camera area in a square tiling with a nominal module–module distance of 200 μm. Taking into account the microcell geometrical fill factor, the effective area of each module amounts to 68.9%. To ensure a positive signal polarity for readout with the front end electronics (FEE)

[1] https://www.cta-observatory.org/

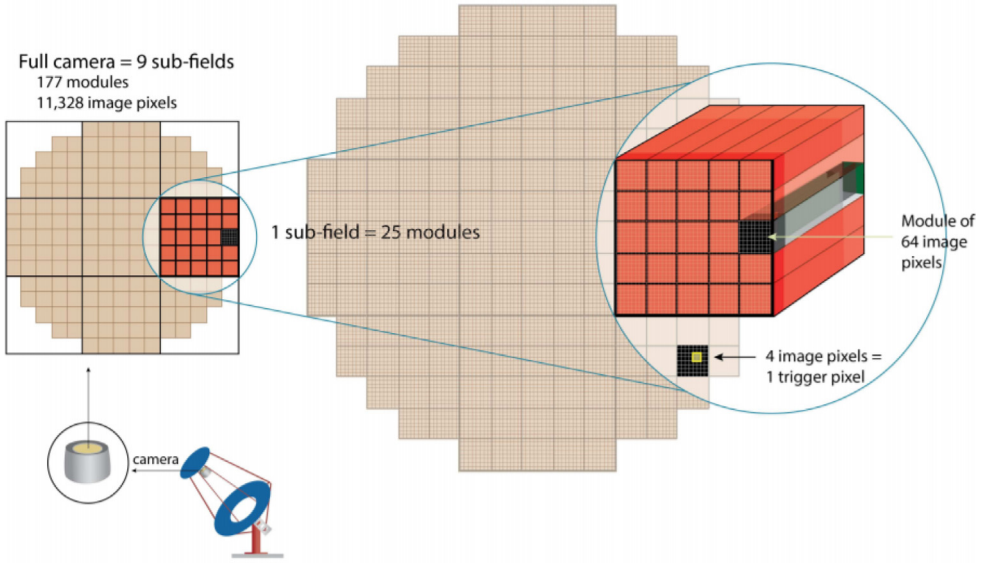

Fig. 1. Schematic of the camera focal plane [7]. The whole camera can be subdivided in 9 sections (black squares on the left), designed to host up to 25 PDUs (smaller squares). Each PDU hosts 64 image pixels, arranged in 4 optical modules.

and digitization board, a common positive bias voltage is provided to the SiPM substrate (cathode), while 16 separate signals are read-out by the SiPM anodes via wire bonds.

The backside of the PCB hosts the connector that supplies the external voltage and that interfaces the 16 SiPM anode signals with the FEE; a copper block is used to mechanically and thermally couple the PCB with the pSCT camera module. The top side of the PCB hosts the SiPMs. A wire-bond connection is used to couple the SiPM anode to the readout pad, as described in detail later. The nominal gap between the sensors after their installation on the PCB amounts to 420 μm, which is compatible with the dimensions of the wedge of the bonding machine used to wire-bond the SiPM bonding pads to the PCB bonding pads.

Two different symmetric layouts of the PCB backside have been produced for compatibility with the pSCT mechanics: each PDU consists of 2 tiles with "Left" symmetry (L) and 2 tiles with "Right" symmetry (R), as shown in Fig. 2. All the PCBs are compatible with the mechanical design of the pSCT camera.

3. Assembly of SiPM arrays

To achieve an accurate alignment of the sensors during the assembly procedures, the SiPMs were manually transferred from the tapes to holder boxes with a vacuum pen. The PCBs were connected to a transportation and gluing jig to ensure stability, robustness, and alignment during the subsequent phases. A manual die-bonder machine was used to first deposit the conductive glue on the pads of the PCB and to subsequently extract the SiPMs from the transportation holders and place them on the pads. We repeated the same procedure using a manual approach, achieving the same level of accuracy in the placement precision.

We placed the sensors according to the geometry discussed in Section 2, with a sensor–sensor distance on the Y view of $\simeq 510\,\mu m$ (see Fig. 3 for the orientation of X and Y). On the X-axis, instead, sensors were placed with a shift of $\simeq 80\,\mu m$ away from the corridor containing the bonding pads on the PCB, to improve the safety margin for the wire-bonding procedure. The alignment of the sensors was optically inspected using an optical micrometer precision metrology machine.

The homogeneity of the alignment within single modules is of the order of 30 μm, while the spread in the average sensor–sensor distance for the whole production is of the order of 30 μm for the X view and 10 μm for the Y view. The average rotation of sensors with respect to the nominal position is negligible, with a level of homogeneity within

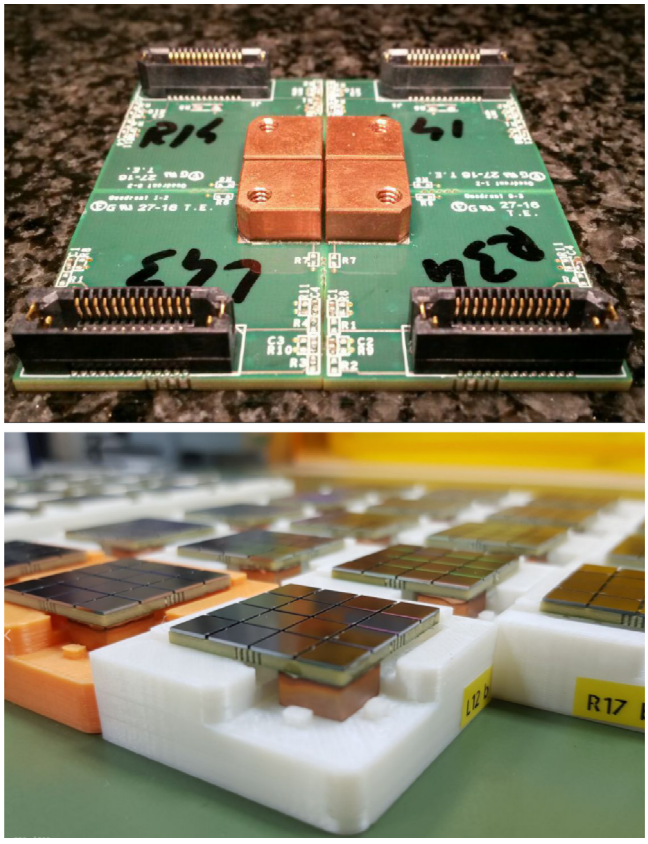

Fig. 2. Top: Backside of four modules, arranged as plugged to one PDU. Bottom: top view of an assembled SiPM array ready for the electrical tests. In the top panel, the two different symmetric layouts of the PCB backside, the "Left" and the "Right" design, can be seen.

single modules of the order of 0.2°. Furthermore, we inspected the planarity of the sensor after the assembly on the PCB using a ruby-head touch probe machine on a pre-production test. The maximum deviation from flatness of the sensor surface observed across the whole modules amounts to 80 μm. The average rotation of single sensors in

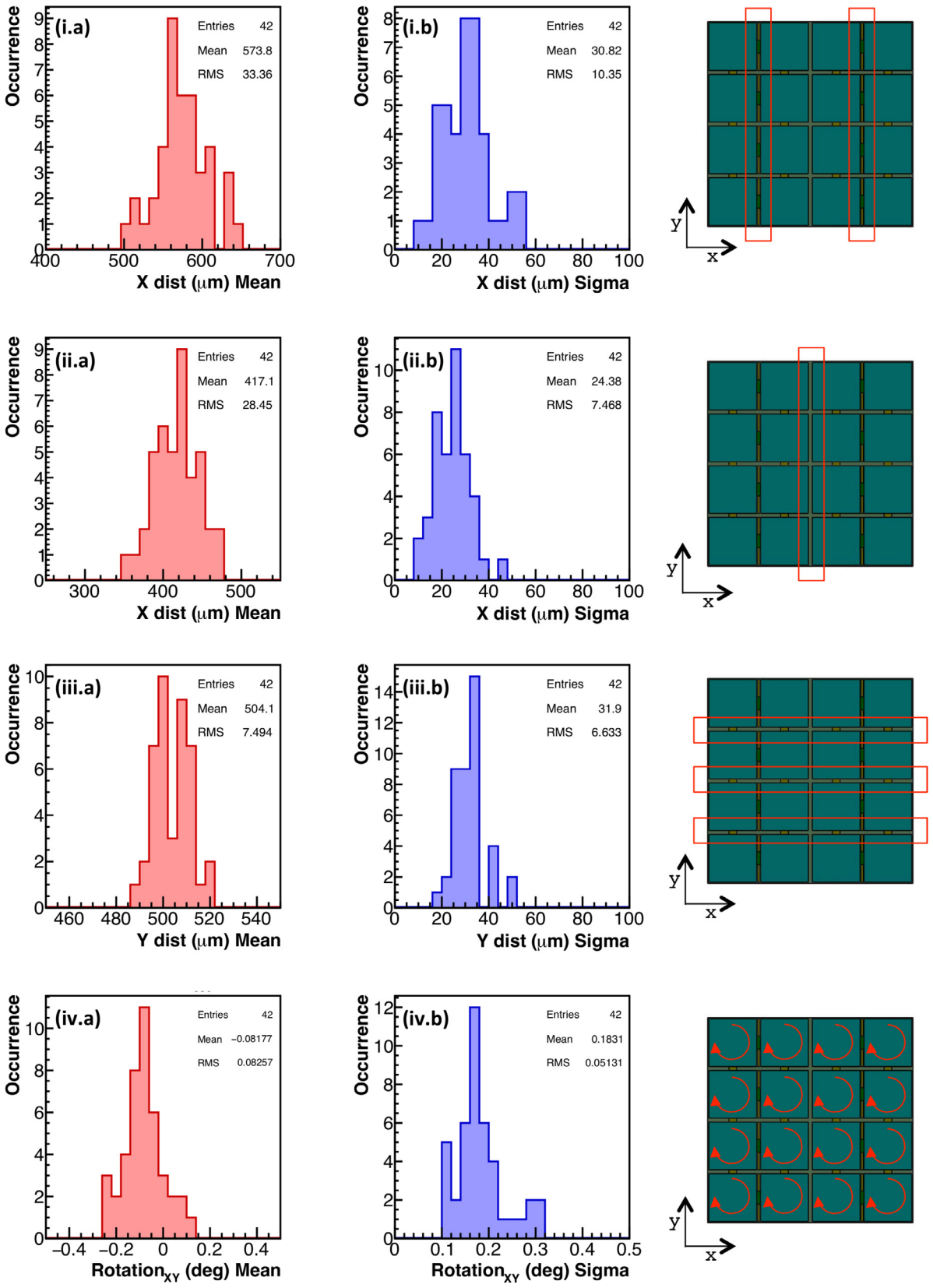

Fig. 3. Result of the optical inspection of 42 modules equipped with sixteen $6 \times 6\,\mathrm{mm}^2$ SiPMs. For each module, we report the mean value (a) and the standard deviation (b) for the distributions of: (i) distance between adjacent sensors in the X view separated by bonding pads, lateral corridors; (ii) distance between adjacent sensors in the X view not separated by bonding pads, central corridor; (iii) distance between adjacent sensors in the Y view; (iv) rotation of the sensor in the XY plane with respect to the PCB axes. The third column is a schematic representation of the quantities measures in each histogram.

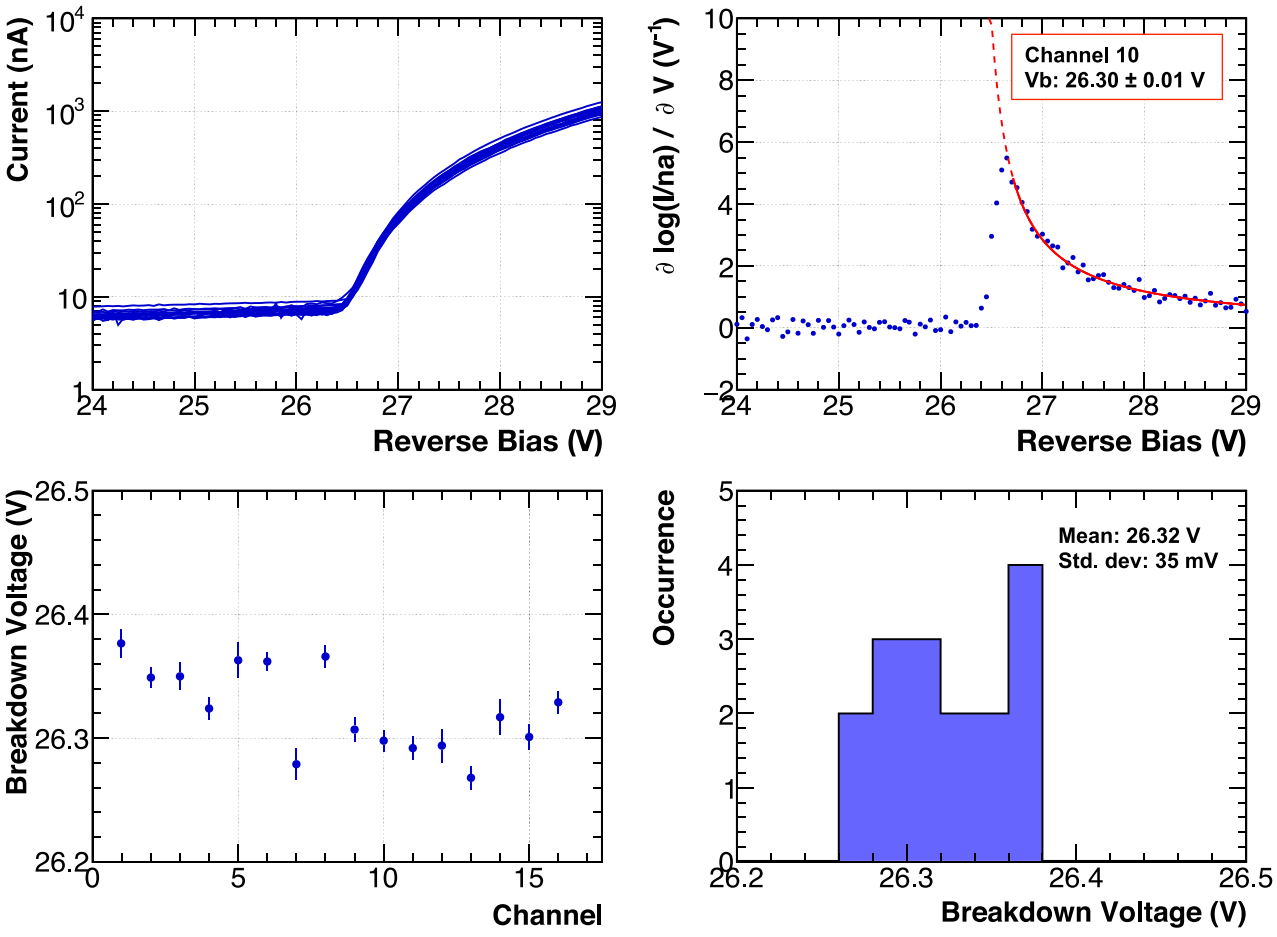

Fig. 4. Example and results of the breakdown voltage measurement for 16 channels of one SiPM array. Top left: IV curves for the 16 channels. Top right: fit of Eq. (1) to the derivative of the logarithm of the current for one channel. Bottom left: measurement of the breakdown voltage for the 16 channels. Bottom right: distribution of the breakdown voltage measurements for the 16 channels.

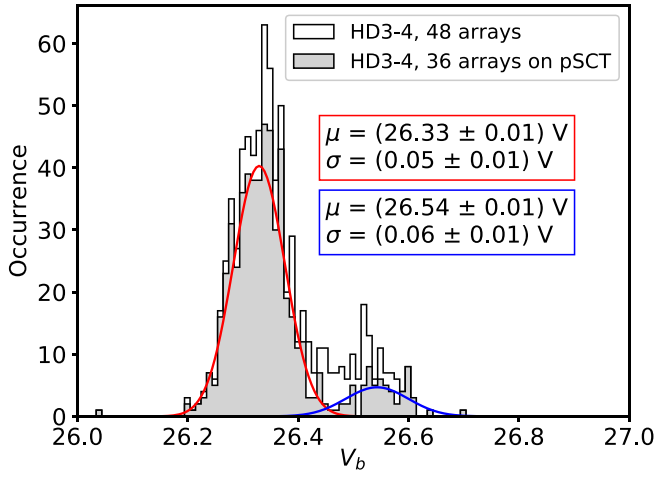

Fig. 5. Distributions of the breakdown voltage for all the 48 SiPM arrays equipped with HD3-4 SiPMs (white) and for the 36 arrays installed on the pSCT camera (gray). The distribution of the arrays installed on the camera was fitted with two gaussian, one for each substrate of the SiPM production.

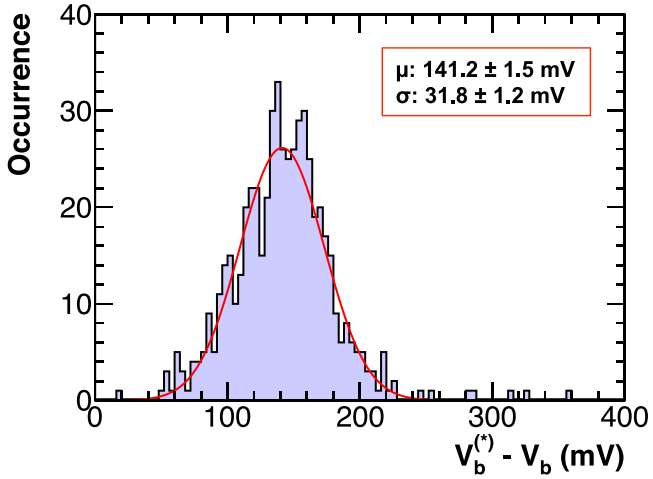

Fig. 6. Distribution of the difference between the breakdown voltage measurements based on the two methods described in the text for 576 SiPMs of the 36 arrays selected to be equipped on the pSCT camera.

the XZ and YZ planes (i.e., a tilt with respect to the nominal XY plane) amounts to 0.2° distributed all over the modules. The results of the optical inspection of a batch of 42 units are shown in Fig. 3.

After assembly, each SiPM anode bonding pad ($0.10\times0.15\,\mathrm{mm}^2$) was bonded using a 25 μm AlSi 1% wire to the signal readout pad of the PCB ($0.3\times2.3\,\mathrm{mm}^2$). The bonding parameters were optimized in order to have a breaking force larger than 9 gf during destructive pull tests. The top

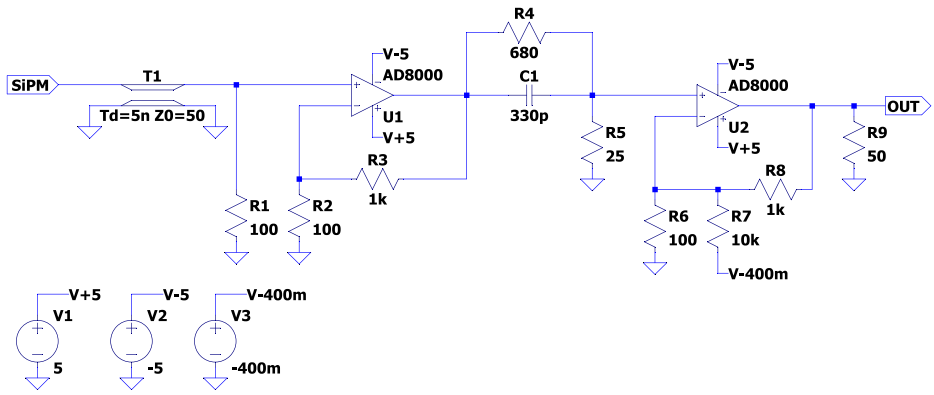

Fig. 7. Schematic of one amplifier channel.

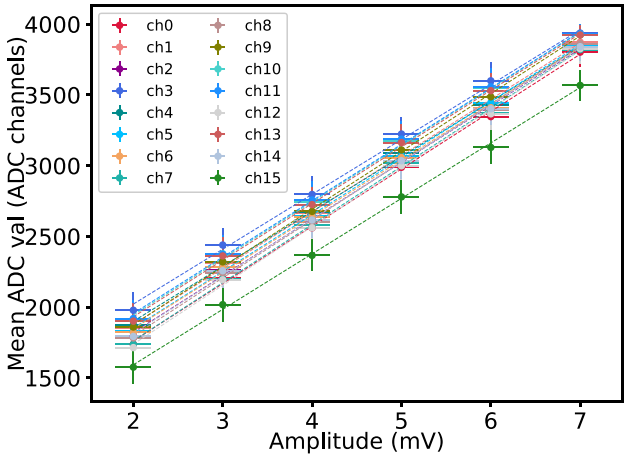

Fig. 8. Calibration curves of the 16 QDC channels. Values of the best fit lines were used to calibrate the SiPM array acquisitions. Different line colors refer to different QDC channels.

of the arch formed by the wire results to be at least 250 μm above the surface of the SiPMs to avoid electrical shorts.

3.1. Electrical tests of SiPM arrays

After assembly, we tested the quality of the SiPM sensors on each module by measuring the current drain of the sensor as a function of the reverse bias voltage, leading to the well-known voltage–current (IV) characteristic. The IV characteristics of all the pixels were used to evaluate the breakdown voltage V_b of each pixel and to evaluate all their properties as a function of the over-voltage (OV) applied, defined as $V_{OV} = V_{bias} - V_b$, where V_{bias} is the bias voltage provided.

A Keithley 2400 Sourcemeter was used to provide the reverse bias to the sensors placed in a dark box and to measure the current at the SiPM anode. An example of IV curves for 16 sensors of a module is shown in Fig. 4, top left panel.

The average sensor shows a current drain of approximately 5 − 10 nA for bias voltages below the breakdown voltage V_{BD} and an exponential increase above the breakdown voltage. To evaluate the value of V_{BD} for each sensor, we applied the procedure explained in [18] based on the analysis of the derivative of the logarithm of the current $I(V_{bias})$ as a function of the bias voltage V_{bias}, which can be parameterized as

$$\frac{\partial \log(I(V_{bias}))}{\partial V_{bias}} = \frac{2}{V_{bias} - V_b}. \quad (1)$$

The value of V_b is retrieved for each SiPM as the best fit value of Eq. (1). An example of the fit procedure for one channel is shown in Fig. 4, top right panel, together with the distribution of the measurements for the 16 channels of one SiPM array, bottom panels.

The procedure was performed on all the SiPM arrays produced. The three productions of FBK NUV-HD SiPMs, namely HD3-2, HD3-3 and HD3-4, differ by the average value of the breakdown voltage in an interval smaller than 1 V while the spread of the breakdown voltage value that is always below 80 mV. The distributions of the measured breakdown voltage at room temperature (≃ 25 °C) for the HD3-4 SiPM arrays is shown in Fig. 5, where the values of the breakdown voltages of the 36 SiPM arrays installed on the pSCT camera are highlighted in gray. The distribution of the arrays installed on the camera was fitted with two Gaussian functions, one with mean $\mu = (26.33 \pm 0.01)$ V and standard deviation $\sigma = 0.05 \pm 0.01$ V and the other with $\mu = 26.54 \pm 0.01$ V and $\sigma = (0.06 \pm 0.01)$ V. The uniformity of the distributions is 0.19% and 0.23% respectively. The difference is probably due to the fact that the SiPMs come from different Si wafers.

We emphasize that Eq. (1) is an operative parametrization to retrieve the breakdown voltage. To verify the robustness of the procedure, we also measured the breakdown voltage as the intersection of two parametrizations of the current: a linear fit to $\log(I(V_{bias}))$ below the current rise, and a 2nd order polynomial fit to $\log(I(V_{bias}))$ above the current rise. This approach provides a measurement of the breakdown voltage $V_b^{(*)}$ that is slightly larger than the one obtained before. As shown in Fig. 6, the average difference obtained by the application of the two procedures on the 576 SiPMs on the 36 arrays installed on the camera amounts to approximately 140 mV with a spread of approximately 30 mV. The difference between the breakdown voltages obtained with the two methods results in negligible variation of the SiPM performance in terms of gain and photon detection efficiency. For all the calculations in the following sections, we considered the breakdown voltages obtained with the fit of the derivative of $log(I(V_{bias}))$.

4. Uniformity tests

After the assembly and the measurement of the breakdown voltage of all the pixels, we tested the performance and the uniformity of the arrays in terms of gain, SNR, and DCR of each SiPM. The setup used to characterize the performance consisted of a frontend board followed by a charge-to-digital converter module (CAEN V792 QDC module). The front-end board consists in an *ad-hoc* 16-channel FEE designed by INFN Napoli, which includes a pole-zero cancellation network in order to filter the long tail of the SiPM signals and increase the signal-to-noise ratio of the integrated signal distributions by removing accidental pileup with the DCR [19]. Fig. 7 shows the schematic of the circuit.

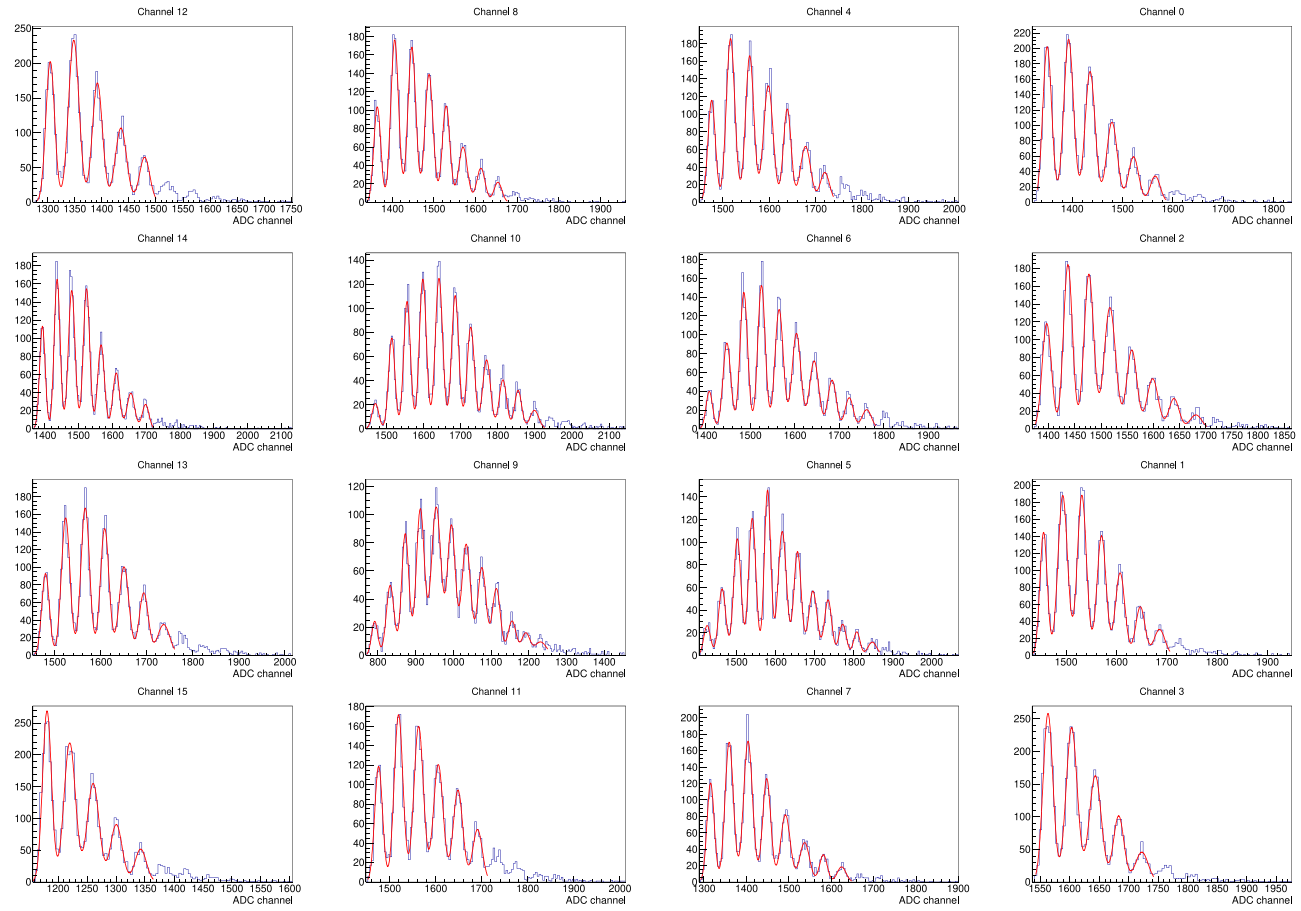

Fig. 9. Integrated signal distributions of the signal of the 16 channels of one SiPM array biased at 33 V, illuminated with a 380 nm Pulsed Diode Laser. The integration time is 50 ns. The red line on each histogram is a multi-gaussian fit superimposed on data. The x-axes in each plot represent the ADC counts, while the y-axes represent the number of entries. The position of each histogram corresponds to the physical position of the SiPM in the array.

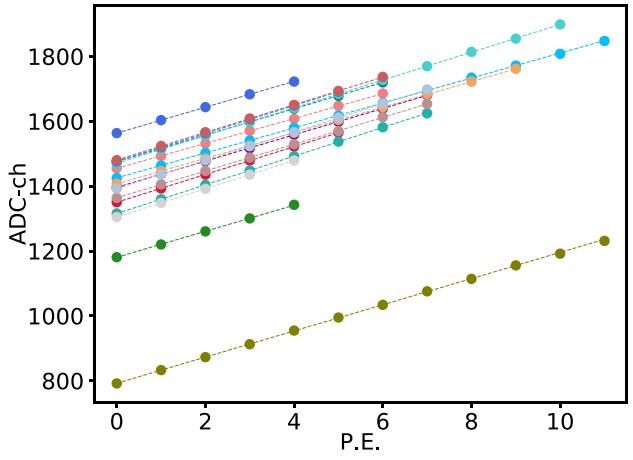

Fig. 10. Peak position (mean of Gaussian distribution) in ADC channels as a function of the p.e. number for the 16 pixels of one SiPM array biased at 33 V, with linear fit superimposed on experimental data. The slope of the curve represents the gain of the system for each p.e. The reduced χ^2 values range from 0.01 to 0.92. Different line colors refer to different pixels according to the same legend in Fig. 8.

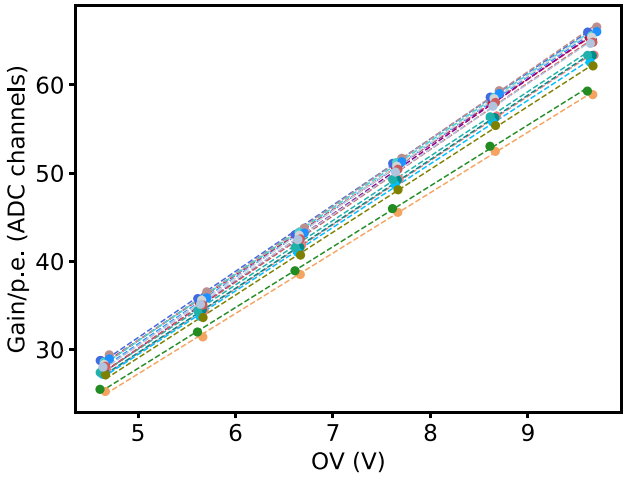

Fig. 11. Gain/p.e. for each of the 16 pixels composing an SiPM array, reported as a function of the over-voltage applied with a linear fit superimposed on experimental data. The reduced χ^2 values range from 0.29 to 3.84. Different line colors refer to different pixels according to the same legend in Fig. 8.

4.1. Setup calibration

Before testing the SiPM arrays, the 16-channels FEE coupled with the QDC module were calibrated with a test signal. The same signal was sent independently to each channel and the output signal of the QDC was collected with the same integration time that was later used to collect the SiPMs signal. We changed the amplitude of the input signal to take into account the different pedestal and conversion factors of the 16 channels, as reported in Fig. 8. This procedure was useful to cross calibrate the 16 channels. We did not apply an absolute calibration,

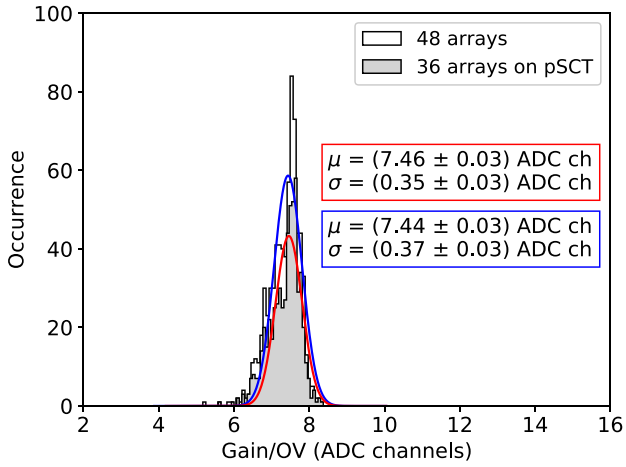

Fig. 12. Distribution of the gain per over-voltage unit for all the 48 optical modules equipped with HD3-4 SiPMs (white) and for the 36 arrays installed on the pSCT camera (gray). Both distributions were fitted with a gaussian function. For the distribution of all the pixels, the mean of the gaussian (blue line) is $\mu = (7.44 \pm 0.03)$ ADC ch/V and the standard deviation is $\sigma = (0.37 \pm 0.03)$ ADC ch/V, while for the distribution of the 576 pixels installed on the pSCT camera the mean of the gaussian (red line) is $\mu = (7.46 \pm 0.03)$ ADC ch/V and the standard deviation is $\sigma = (0.35 \pm 0.03)$ ADC ch/V. The uniformity of the latter histogram is 4.7%.

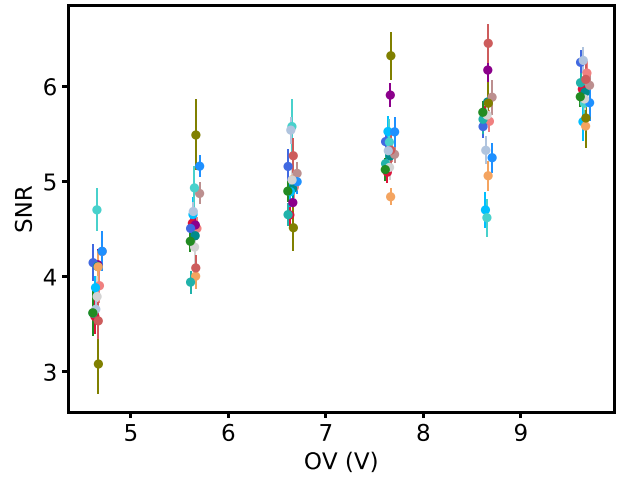

Fig. 13. Single p.e. signal-to-Noise ratio for all the channels in a SiPM array as a function of the applied over-voltage. Different line colors refer to different pixels according to the same legend in Fig. 8.

so we did not measure the charge corresponding to the single photo-electron (p.e.) of the SiPMs. This aspect is beyond the aim of this work.

4.2. Experimental results on uniformity tests

We tested each array with bias voltage ranging from 31 V to 36 V ($\simeq$ 4.5 − 9.5 V of OV) in steps of 1 V, illuminating them with a 380 nm Pulse Diode Laser. A diffusing lens was placed between the laser head and the detector to irradiate all pixels. We also acquired data in dark conditions (i.e. without the pulsed laser) to acquire the integrated signal in absence of light. The integration time was fixed at 50 ns in order to integrate only the signal induced by the laser light. We performed all measurements at room temperature, $T \simeq 25$ °C.

We obtained the integrated signal distribution for each SiPM array and analyzed them in order to obtain the integrated charge per p.e. and the SNR of the first p.e. for each of the 16 pixels. Data taken under dark conditions were analyzed to evaluate the DCR for each pixel, as is explained later in this work. An example of the fitted integrated signal distribution for one SiPM array of the FBK HD3-4 batch at a given bias voltage ($V_{\text{bias}} = 33$ V) is reported in Fig. 9. The position of each histogram corresponds to the physical position of the SiPM in the array. As can be seen, the central pixels show a higher average number of p.e. due to a imperfectly uniform illumination.

The first peak of the distributions corresponds to the absence of any pulse from the laser, while the second one corresponds to the detection of one p.e., the third to two p.e., and so on. As can be seen from the distributions, all spectra follow a compound Poissonian distribution which reflects the probability to observe pulses equal to $0, 1, \ldots n$ fired microcells in a single pixel, taking into account the cross-talk probability [20]. Each peak has a Gaussian distribution due to excess noise of charge multiplication, structural differences between microcells in the individual SiPM, and noise introduced by the readout electronics. Each spectrum was fitted with a multi-gaussian function in the form:

$$\mathcal{M}(x) = \sum_{i=0}^{N} f_i \, \mathcal{G}(x, \mu_i, \sigma_i), \tag{2}$$

where x is the central value of the charge histogram bin, $\mathcal{G}(x, \mu_i, \sigma_i)$ is the Gaussian distribution with mean μ_i and width σ_i of the $i-$th peak and f_i is its normalization factor of each peak. The sum runs up to an arbitrary number N that represents the maximum number of fired pixels that is statistically significant.

The parameters from the multi-Gaussian fit were extracted for each number of p.e.s to quantify the performance of the devices. In particular, we evaluated the trend of the mean μ_i as a function of the number of photons detected, which shows a linear behavior, as reported in Fig. 10 for one of the arrays biased at 33 V.

The slope of each best fit line in Fig. 10 gives information about the gain of the system, i.e. SiPM and amplification stage, for each bias voltage considered. We then combined this information with the breakdown voltages for each channel to evaluate the gain as a function of the OV, as shown in Fig. 11 for one of the SiPM arrays.

We performed a linear fit on each of the curves, obtaining the gain per over-voltage unit for each of the pixels. The distribution of the gain/V for all the HD3 pixels tested is reported in Fig. 12 as a white histogram. The gray histogram represents the distribution of the gain/V only for the pixels installed on the pSCT camera. Both histograms were fitted with a gaussian function. For the distribution of all the pixels, the mean of the gaussian is $\mu = (7.44 \pm 0.03)$ ADC ch/V and the standard deviation is $\sigma = (0.37 \pm 0.03)$ ADC ch/V, while for the distribution of the 576 pixels installed on the pSCT camera the mean of the gaussian is $\mu = (7.46 \pm 0.03)$ ADC ch/V and the standard deviation is $\sigma = (0.35 \pm 0.03)$ ADC ch/V. The uniformity of the distribution of the pixels installed on the pSCT camera is 4.7%. No significant differences have been found between the two distributions.

The collected data were also analyzed to evaluate the SNR of the system at different voltages. The SNR compares the level of detectable signals to the level of background noise. The SNR of each peak can be estimated through following relation:

$$SNR_i = \frac{\mu_i - \mu_0}{\sigma_0} \tag{3}$$

with μ_i and μ_0 being respectively the position of the $i-$th peak in the charge distributions reported in Fig. 9 and the pedestal position, and σ_0 the standard deviation of the pedestal.

The trend of the quantities SNR_i versus the ith p.e. detected was then fitted with a linear function for each channel at each bias voltage, with the slope representing the SNR for the single p.e. (simply named SNR hereafter). These values are reported in Fig. 13 as a function of the applied over-voltage. It can be seen that the SNR of the system increases with the over-voltage but is not linear. This behavior can be expected due to the increase of intrinsic noise, which spoils the separation of the p.e. peaks.

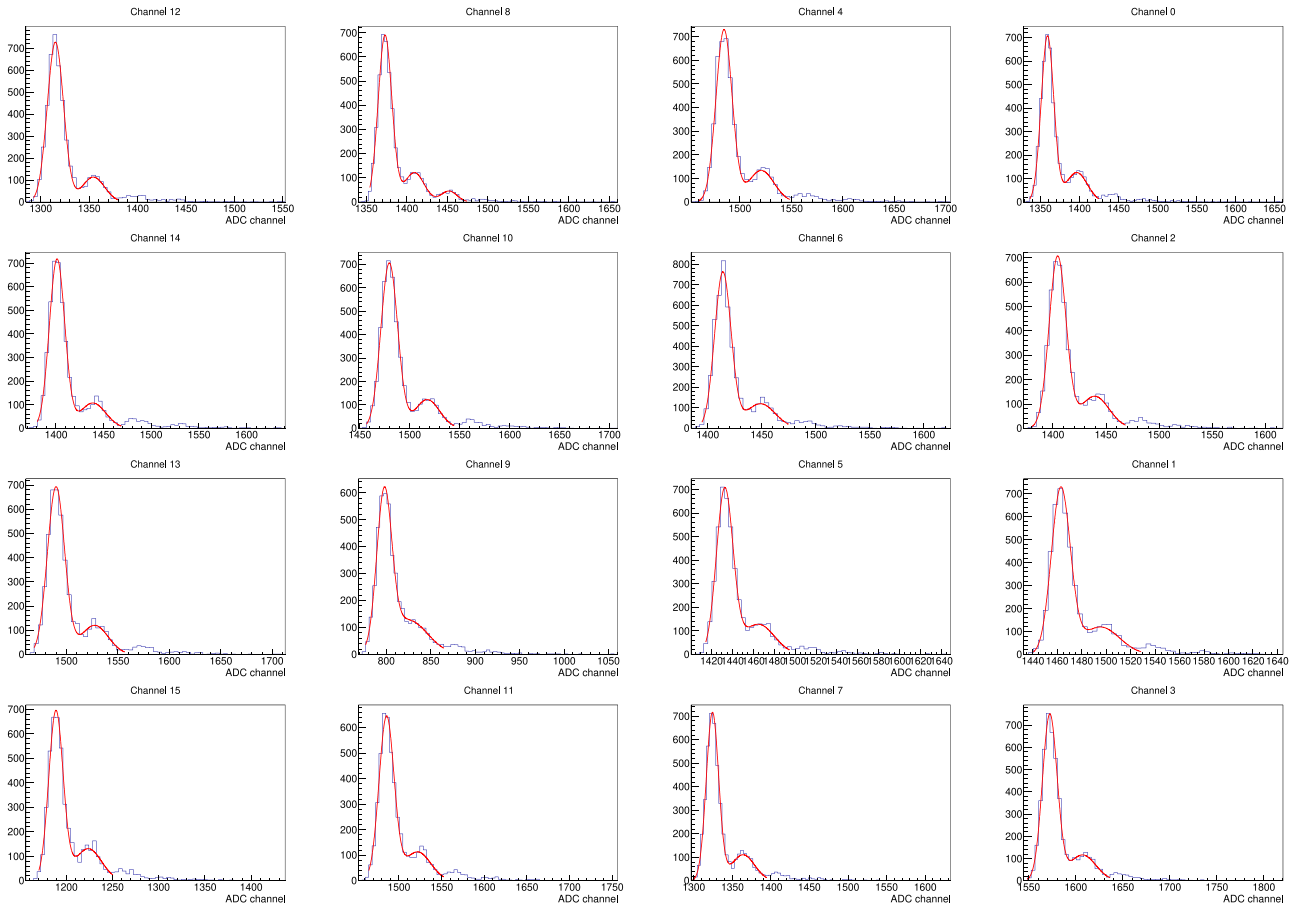

Fig. 14. Integrated signal distribution of the signal under dark conditions of the 16 channels of one SiPM array, biased at 33 V. The integration time is 50 ns. The red line on each histogram is a multi-gaussian fit.

We note that the mean SNR among all the pixels tested is ~ 5 at $V_{\text{bias}} = 34$ V, corresponding to $V_{\text{OV}} \sim 7.6$ V.

In order to measure the dark count rate of each pixel at different OV values, we conducted measurements on the SiPM arrays also in absence of light. The DAQ chain was the same as the one described for the measurements performed with the laser turned on. SiPM array signals were acquired with the QDC to obtain the integrated charge over a 50 ns time interval. Fig. 14 shows the charge spectra obtained for one SiPM array at bias voltage 33 V.

The spectra are characterized by a high peak corresponding to the absence of any pulses in the time window considered, followed by one or two smaller peaks corresponding to the first or second p.e. These p.e. signals are due to dark counts which occur in the considered integration window.

We obtained the dark count rate for each channel adopting the following formula:

$$DCR = \frac{\ln\left(N_{\text{tot}}/N_0\right)}{\Delta t}, \tag{4}$$

where N_{tot} is the total number of events acquired during the integration window, N_0 is the number of pedestal events (i.e. no photon signal), evaluated as the area of the fitted pedestal gaussian, and Δt is the integration time in each event. The trend of the DCR as a function of the over-voltage for one of the arrays is reported in Fig. 15 with a linear fit superimposed on experimental data.

As we did for the gain, we collected the slope parameters of the curves reported in Fig. 15, repeating the procedure for each pixel. The distribution of the DCR/OV unit for all the pixels tested is reported in Fig. 16 (white histogram), with the distribution of the DCR/OV of the arrays installed on the pSCT camera shown in gray. A Gaussian fit was

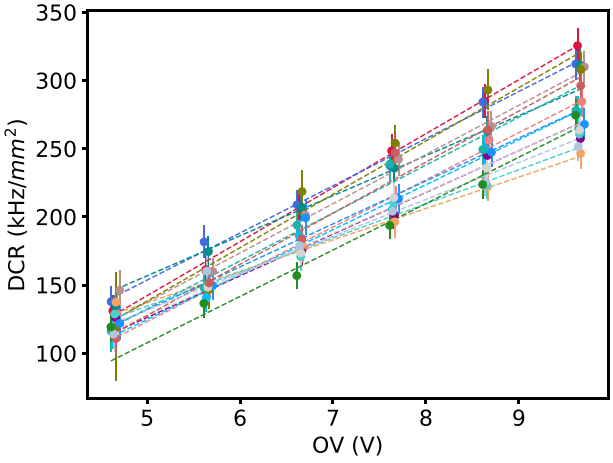

Fig. 15. Dark values for each channel in a single SiPM array as a function of the over-voltage applied. A linear fit is shown superimposed on data. The reduced χ^2 values range from 0.03 to 1.22. Different line colors refer to different pixels according to the same legend in Fig. 8.

performed on both distributions. For the distribution of all the pixels, the mean of the gaussian (blue line) is $\mu = (32.0 \pm 0.1)\,\text{kHz/mm}^2/\text{V}$ and the standard deviation is $\sigma = (5.7 \pm 0.1)\,\text{kHz/mm}^2/\text{V}$. For the distribution of the pixels installed on the camera, the mean value of DCR/OV of the distribution is $(32.2 \pm 0.2)\,\text{kHz/mm}^2/\text{V}$ with a standard deviation $(5.4 \pm 0.2)\,\text{kHz/mm}^2/\text{V}$. The value of the DCR at 6–7V of over-voltage

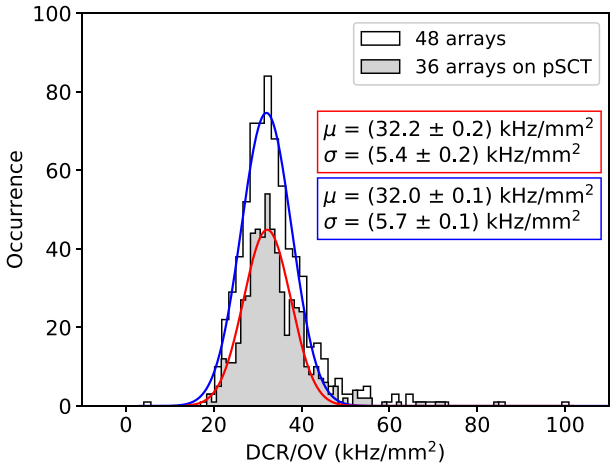

Fig. 16. Distribution of the dark-count-rate per over-voltage unit for all the 48 optical modules equipped with HD3-4 SiPMs (white) and for the 36 arrays installed on the pSCT camera (gray). Both distributions were fitted with a gaussian function. For the distribution of all the pixels, the mean of the gaussian (blue line) is $\mu = (32.0 \pm 0.1)\,\mathrm{kHz/mm^2/V}$ and the standard deviation is $\sigma = (5.7 \pm 0.1)\,\mathrm{kHz/mm^2/V}$, while for the distribution of the 576 pixels installed on the pSCT camera the mean of the gaussian (red line) is $\mu = (32.2 \pm 0.2)\,\mathrm{kHz/mm^2/V}$ and the standard deviation is $\sigma = (5.4 \pm 0.2)\,\mathrm{kHz/mm^2/V}$. The uniformity of the latter histogram is 13.9%.

Table 1
Summary of performance of the 36 arrays installed on the pSCT camera.

	Mean	Standard deviation
V_{BD} (V) (first group)	26.33	0.05
V_{BD} (V) (second group)	26.54	0.06
Gain (ADC channels/OV unit)	7.5	0.4
SNR at OV=6.5 V	4.9	0.2
DCR (kHz/mm^2/V)	32.2	5.4

is about 6.5 MHz/pixel, which is one order of magnitude smaller than the rate of the night sky background.

5. Conclusions and outlook

We assembled and tested different productions of FBK NUV-HD3 SiPMs. Among the different production of HD SiPM developed, HD3-4 SiPM arrays showed better and more uniform performance and were chosen to equip the camera of pSCT. The performance of these arrays are summarized in Table 1. After the characterization tests performed on the HD3-4 arrays, 36 arrays were selected to be coupled to the front-end electronics of the pSCT camera [21].

The 36 selected arrays were aligned on 9 FEE modules using special copper elements to set the correct curvature in each camera sector. After the alignment procedure, the 9 modules were installed on the pSCT camera in Arizona in December 2018. The prototype was inaugurated in January 2019. Even with only one equipped sector of its camera, the pSCT is providing important information on the procedures for the optical alignment and the camera operation and calibration, while proving the viability of the novel telescope design in gamma-ray astrophysics thanks to the first campaign of observations which led to the detection of TeV gamma-ray emission from the Crab Nebula [22]. The characterization results presented in this work are essential to study the performance of the pSCT both with dedicated simulations and real data.

An upgrade of the pSCT camera is foreseen over the next few years. The full focal plane is expected to be equipped entirely with FBK NUV-HD3 SiPMs, for a total of 11 328 pixels, increasing the FoV from 2.68° to almost 8°. A detailed characterization of the full production of the new SiPM arrays for the upgraded camera will be performed before the integration with the electronic chain. Moreover, also the FEE will be upgraded to use of three dedicated ASICs for the pre-amplification, the digitization, and the trigger stages [23].

Declaration of competing interest

The authors declare that they have no known competing financial interests or personal relationships that could have appeared to influence the work reported in this paper.

Data availability

Data will be made available on request.

Acknowledgments

This research was supported by grants from the Istituto Nazionale di Fisica Nucleare (INFN) in Italy and the U.S. National Science Foundation and the Smithsonian Institution in the USA. The authors gratefully acknowledge the Italian National Grant TECHE.it funded by the Italian Ministry of Education. The authors also acknowledge A. Gola, G. Paternoster and G. Borghi of Fondazione Bruno Kessler for many fruitful discussions and collaboration. L.D. acknowledges the initiative "Research for Innovation (REFIN) - codice progetto 73A60A91" financed by Regione Puglia, Italy. The development, construction, and operation of the pSCT was supported by NSF awards (PHY-1229792, PHY-1229205, PHY-1229654, PHY-1913552, PHY-1807029, PHY-1510504, PHY-1707945, PHY-2013102, PHY-1707544, PHY-2011361, PHY-1707432, PHY-1806554, PHYS-1607491, PHYS-1913798, PHY-1828168 and PHY-2011420) together with funds from Barnard College, USA, California State University East Bay, USA, Columbia University, USA, Georgia Institute of Technology, USA, Iowa State University, USA, Smithsonian Institution, USA, Stanford University, USA, University of Chicago, USA, University of Alabama in Huntsville, USA, University of California, USA, University of Iowa, USA, University of Utah, USA, University of Wisconsin–Madison, USA, and Washington University in St. Louis, USA.

References

[1] C. Consortium, B.S. Acharya, I. Agudo, et al., Science with the Cherenkov Telescope Array, 2019, http://dx.doi.org/10.1142/10986.
[2] G. Maier, L. Arrabito, K. Bernlöhr, et al., Performance of the Cherenkov Telescope Array, Vol. 301, 2017, p. 846, arXiv:1709.01381.
[3] M. Actis, G. Agnetta, F. Aharonian, et al., Design concepts for the Cherenkov Telescope Array CTA: an advanced facility for ground-based high-energy gamma-ray astronomy, Exp. Astron. 32 (3) (2011) 193–316, http://dx.doi.org/10.1007/s10686-011-9247-0, arXiv:1008.3703.
[4] G. Pühlhofer, The medium size telescopes of the cherenkov telescope array, in: 6th International Symposium on High Energy Gamma-Ray Astronomy, in: American Institute of Physics Conference Series, Vol. 1792, 2017, 080002, http://dx.doi.org/10.1063/1.4969023, arXiv:1610.02899.
[5] K.J. Meagher, Schwarzschild-couder telescope for the cherenkov telescope array, in: L.M. Stepp, R. Gilmozzi, H.J. Hall (Eds.), Ground-Based and Airborne Telescopes V, in: Society of Photo-Optical Instrumentation Engineers (SPIE) Conference Series, Vol. 9145, 2014, 914533, http://dx.doi.org/10.1117/12.2054979, arXiv:1407.3271.
[6] V.V. Vassiliev, S.J. Fegan, Schwarzschild-couder two-mirror telescope for ground-based γ-ray astronomy, in: International Cosmic Ray Conference, in: International Cosmic Ray Conference, Vol. 3, 2008, pp. 1445–1448, arXiv:0708.2741.
[7] A.N. Otte, J. Biteau, H. Dickinson, et al., Development of a SiPM camera for a Schwarzschild-Couder Cherenkov telescope for the cherenkov telescope array, 2015, arXiv e-prints arXiv:1509.02345.
[8] D. Nieto, T.B. Humensky, P. Kaaret, et al., Prototype 9.7 m Schwarzschild-Couder telescope for the Cherenkov telescope array: status of the optical system, 2017, arXiv e-prints arXiv:1709.06324.
[9] C.B. Adams, G. Ambrosi, M. Ambrosio, et al., Prototype Schwarzschild-couder telescope for the Cherenkov telescope array: Commissioning the optical system, 2021, arXiv e-prints arXiv:2110.07463.
[10] G. Ambrosi, M. Ambrosio, C. Aramo, et al., Development of a SiPM Cherenkov camera demonstrator for the CTA observatory telescopes, Nuovo Cim. C 40 (1) (2017) 78, http://dx.doi.org/10.1393/ncc/i2017-17078-5, arXiv:1612.08605.

[11] C. Piemonte, A new Silicon Photomultiplier structure for blue light detection, Nucl. Instrum. Methods Phys. Res. A 568 (2006) 224–232, http://dx.doi.org/10.1016/j.nima.2006.07.018.

[12] T. Pro, A. Ferri, A. Gola, et al., New developments of near-UV SiPMs at FBK, IEEE Trans. Nucl. Sci. 60 (3) (2013) 2247–2253, http://dx.doi.org/10.1109/TNS.2013.2259505.

[13] A. Gola, F. Acerbi, M. Capasso, et al., NUV-sensitive silicon photomultiplier technologies developed at fondazione bruno kessler, Sensors 19 (2) (2019) http://dx.doi.org/10.3390/s19020308, URL https://www.mdpi.com/1424-8220/19/2/308.

[14] G. Ambrosi, E. Bissaldi, N. Giglietto, et al., Silicon photomultipliers and front-end electronics performance for cherenkov telescope array camera development, Nucl. Instrum. Methods Phys. Res. A 845 (2017) 8–11, http://dx.doi.org/10.1016/j.nima.2016.04.050, Proceedings of the Vienna Conference on Instrumentation 2016.

[15] G. Ambrosi, E. Bissaldi, N. Giglietto, et al., An upgrade of the camera focal plane of a Schwarzschild couder telescope prototype (pSCT) for the cherenkov telescope array (CTA), Nucl. Part. Phys. Proc. 291–293 (2017) 48–51, http://dx.doi.org/10.1016/j.nuclphysbps.2017.06.011, URL https://www.sciencedirect.com/science/article/pii/S2405601417303905.

[16] G. Ambrosi, M. Ambrosio, C. Aramo, et al., Characterization of FBK NUV-HD SiPMs for the pSCT camera proposed for the Cherenkov telescope array, Nucl. Instrum. Methods Phys. Res. A 936 (2019) 542–544, http://dx.doi.org/10.1016/j.nima.2018.11.030.

[17] G. Ambrosi, et al., High density near ultraviolet silicon photomultipliers: characterization of photosensors for Cherenkov light detection, 2022.

[18] A.N. Otte, D. Garcia, T. Nguyen, D. Purushotham, Characterization of three high efficiency and blue sensitive silicon photomultipliers, Nucl. Instrum. Methods Phys. Res. A 846 (2017) 106–125, http://dx.doi.org/10.1016/j.nima.2016.09.053, arXiv:1606.05186.

[19] G. Ambrosi, M. Ambrosio, C. Aramo, et al., Development of a charge preamplifier to improve NUV-HD SiPM performances, Nucl. Part. Phys. Proc. 291–293 (2016) 40–43, http://dx.doi.org/10.1016/j.nuclphysbps.2017.06.009.

[20] S. Vinogradov, T. Vinogradova, V. Shubin, et al., Probability distribution and noise factor of solid state photomultiplier signals with cross-talk and afterpulsing, in: 2009 IEEE Nuclear Science Symposium Conference Record (NSS/MIC), 2009, pp. 1496–1500, http://dx.doi.org/10.1109/NSSMIC.2009.5402300.

[21] C.B. Adams, G. Ambrosi, M. Ambrosio, et al., Design and performance of the prototype Schwarzschild-Couder telescope camera, J. Astronomical Telescopes, Instrum., Syst. 8 (1) (2022) 1–38, http://dx.doi.org/10.1117/1.JATIS.8.1.014007.

[22] C.B. Adams, R. Alfaro, G. Ambrosi, et al., Detection of the crab nebula with the 9.7 m prototype Schwarzschild-couder telescope, Astropart. Phys. 128 (2021) 102562, http://dx.doi.org/10.1016/j.astropartphys.2021.102562, arXiv:2012.08448.

[23] R. Paoletti, The upgraded camera for the prototype Schwarzschild-Couder Telescope of the Cherenkov Telescope Array, in: T.B. Hull, D.W. Kim, P. Hallibert (Eds.), Astronomical Optics: Design, Manufacture, and Test of Space and Ground Systems II, Vol. 11116, SPIE, International Society for Optics and Photonics, 2019, pp. 73–79, http://dx.doi.org/10.1117/12.2530431.